9

PIV as a Complement to LDA in the Study of an Unsteady Oscillating Turbulent Flow

Chong Y. Wong*, Graham J. Nathan, Richard M Kelso
University of Adelaide,
**Now at CSIRO Process Science and Engineering, Australia*

1. Introduction

In the last decade, particle image velocimetry (PIV) has become a standard laser diagnostic tool in numerous fluid mechanics laboratories worldwide. At first glance, it appears straight-forward to set up an off-the-shelf system for a quick investigation of the flow of interest. However, unless additional effort is taken to understand the flow, results from 'quick investigations' may lead to limited and sometimes spurious interpretation of the physical flow phenomena. This is especially so for highly three-dimensional and turbulent flows. This chapter examines the efficacy of phase-averaged particle image velocimetry results in assessing the physical phenomena occurring in highly periodic flows and how they complement results from phase-averaged laser Doppler anemometry (LDA) and surface flow visualisation techniques. A specific case study will be presented to demonstrate the complementary nature of these techniques.

The selected flow, a fluidic precessing jet, is a turbulent and highly three-dimensional jet that is used as a fluid mixing device in a combustion lance, or "burner", in rotary kilns. It has been found to achieve low-NO_x (Oxides of Nitrogen; a type of Greenhouse gas) emissions as a gas-fired burner, developed by researchers at the University of Adelaide (Luxton & Nathan, 1988). The flow field lowers flame temperatures by reducing flame strain, which enhances soot formation (Nathan et al., 2006). This reduces NO_x emissions by 30-40% in typical cement kilns (Manias & Nathan, 1994) compared with conventional kiln burners (free jet burners), and its enhanced radiation heat transfer also improves the product quality (Manias & Nathan, 1994) and output (Videgar, 1997) of the clinker in rotary cement kilns. Specific fuel savings of approximately 3-6% were typically reported (Videgar, 1997). The patented burner (hereinafter called the 'fluidic precessing jet' or FPJ nozzle) is commercially known as the Gyrotherm™ and is based on a geometrically simple nozzle configuration.

Although the FPJ nozzle is simple in design, the flow within and emerging from the nozzle is unsteady and highly three-dimensional (Fig. 1). Several experimental FPJ nozzles were developed to study the fundamental characteristics of the precessing jet. Some of the experiments employed classical flow visualisation techniques, such as particle-tracing (using glass beads or gas bubbles), shadowgraph, smoke, cotton tufts, coloured dyes and China-clay surface flow visualisations (Nathan, 1988), as well as quantitative methods including

yaw-probe meters, hot-wire anemometers, pressure probes, an entrainment shroud (Nathan, 1988), planar laser induced fluorescence (PLIF), OH-PLIF and particle image velocimetry (PIV) (Newbold, 1997; Nobes, 1997). Nevertheless, many details of the flow structure eluded researchers for some two decades and it is only recently that its phase-averaged flow structure has been revealed through the use of laser diagnostic techniques such as phase-averaged PIV and LDA, complemented by a classical surface flow visualisation technique (Wong, Nathan & Kelso, 2008).

The chapter presents a summary both of the flow field itself and of the approaches used to investigate it. Section 2 provides details of what is known about the fluidic precessing jet flow and explains how a qualitative understandaing of the flow was used to develop a methodology for a systematic investigation of it. Finally section 3 discusses the key results and constructs a qualitative image of the flow based on these results.

2. A case study of an unsteady oscillating turbulent flow

This section presents a case study in the use of PIV to investigate a fluidic precessing jet (FPJ). As discussed earlier, the FPJ produces an unsteady, oscillating turbulent flow with unique fluid mechanical features. In order to apply any laser diagnostic technique, it is necessary to understand the characteristic features of the flow so that an appropriate experimental strategy can be planned.

2.1 Characteristic of a fluidic precessing jet

The FPJ nozzle, introduced above, comprises a cylindrical chamber with a diameter D_1 and a length L (~$3D_1$) with a small axisymmetric inlet (d=15.79mm) at one end and an exit lip (D_2) at the other (Fig. 3). Referring to Fig. 1, the inlet flow forms a central jet which in the jet precession mode, reattaches non-preferentially onto the curved wall of the chamber (Nathan, 1988). As a result of flow instabilities setup within the chamber, the flow precesses around the chamber wall (Nathan & Luxton, 1992). A region of swirl is formed at the upstream end of the chamber, approximately $x/L \leq 1/6$. A larger recirculation region is also observed to feed the swirling region, originating from near to the lip. The fluid in the swirling flow is found to comprise contributions both from the recirculated fluid from the main jet and a typically smaller contribution by induced ambient fluid (Nathan, 1988; Nathan, Hill & Luxton, 1998; Parham, 2000). As the jet exits, it does not completely occupy the exit plane (Nathan & Luxton, 1992). The exit flow is then directed through a large angle (typically θ=45° from the nozzle axis) towards the axis and across the face of the nozzle outlet. The emerging flow is also highly three-dimensional and the precession extends for several chamber diameters downstream from the exit plane (Nathan, 1988).

2.1.1 Mode switching nature

Nathan, Hill and Luxton (1998) reported on the mode-switching behaviour of the precessing jet. They identified two major flow modes: an axial-jet mode and a precessing-jet mode. The corresponding conjectured flow patterns for the flow in either mode are also given in Nathan, Hill and Luxton (1998). When in the axial jet mode, the inlet jet emerges from the exit plane without significantly attaching to the inner walls of the chamber. A symmetric region of recirculating flow on the upper and lower sides of the jet is clearly observed

(Nathan, Hill & Luxton, 1998). Hill (1992) reported that the axial jet mode is greatly suppressed by use of a centrebody positioned near to the exit of the chamber. The presence of a centrebody blocks the path of the axial jet. Consequently, some of the flow becomes re-directed back into the nozzle while the majority of the flow by-passes the centrebody and emerges in an asymmetric fashion from the exit plane resulting in the precessing-jet mode. Therefore, in order to increase the probability of the precessing jet mode for all the phase-averaging experiments, a centrebody arrangement is used in the investigation reported here.

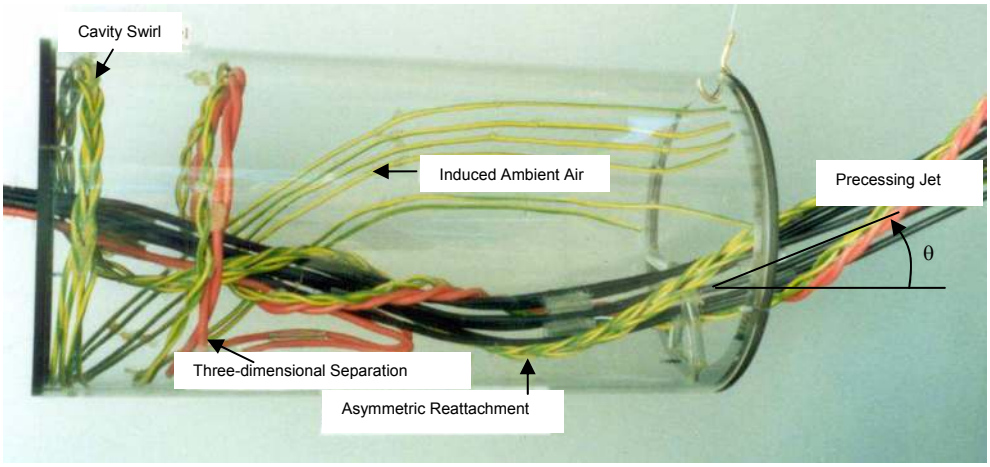

Fig. 1. Perspex-wire model of the conjectured flow topology from flow visualisation studies (reprinted with permission and adapted from Nathan, 1988).

Dependence on inlet flow conditions

Nathan and Luxton (1992) reported that a precessional instability occurs in an axisymmetric duct when the expansion ratio (E=D_1/d) of a sudden expansion at its inlet is sufficiently large (ie. E>5). In addition, they noted that the chamber's length-to-diameter ratio must be about L/D_1=2.7 and that the Reynolds number based on the inlet conditions be sufficiently high, with the precessional instability becoming dominant above a critical value (Re_d>20,000) for precession with a deflected jet to occur. Hill, Nathan and Luxton (1995) investigated, in water, the flow through an axisymmetric large sudden expansion into a long downstream duct. They found that jet precession can be generally described by the axial momentum (M), duct diameter (D_1) and the fluid properties (i.e. density and kinematic viscosity) of the inlet fluid. In quantifying their results for duct diameters of D_1=60mm and D_1=140mm for varying expansion ratios, using a video camera with a framing rate of 30Hz, they visually counted (frame by frame) the frequency of precession by noting the oscillations in the seeded jet in water. Their inlet flow was seeded with 0.6mm diameter neutral-density polystyrene beads. The minimum precession cycle count was N_p=3 for E=3.75 at Re_d=4400 while the maximum count recorded was N_p=107 for E=14.2 at Re_d=56500. The small sample size, used for the low Re_d number experiments, meant that the result was not statistically conclusive. Despite the measurement difficulties, especially for the low Re_d flows, a useful relationship between expansion ratio E and Reynolds number Re_d was established for suddenly-expanded flows into long ducts.

2.1.2 Jet precession and its dependence on nozzle configuration

Mi and Nathan (2000) conducted a parametric study to determine the influence on precession frequency of the systematic variation of key dimensional parameters. Their single stationary hot-wire study concluded that jet precession frequency was mainly a function of the chamber's length-to-diameter, lip-to-diameter, and centrebody-position-to-diameter ratios, further supporting the study conducted earlier by Nathan and Luxton (1992). Other factors included the size of the centrebody (CB), the size of the exit lip, the presence or absence of a CB, and the presence or absence of a lip. They noted that different inlet conditions, such as an orifice or a contraction inlet, also influenced precession frequency.

2.1.3 Variation of exit angles in the emerging precessing jet

Nathan (1988), using flow visualization, documented that the exit angle of the emerging jet (Fig. 1) can vary from θ=30° to θ=60° relative to the geometric centreline. This adds even more variability to the flow and renders measurements in the flow more difficult. The influence of the jet exit angle on the downstream flow has been examined in further detail by Nobes (1997) who used a mechanically-rotated precessing jet (MPJ). He found that increasing the jet exit angle increases the spread of the jet helix and this results in an increase in the initial mixing rate in the jet. For every given angle, there is a critical Strouhal number, above which the jet converges to the axis of rotation and, below which, it does not. For an exit angle of 45°, $St_{p,cr} \sim 0.008$ (Mi and Nathan, 2005), where $St = f_p\, d_e \,/\, u_e$, where f_p is the frequency of precession, d_e is the nozzle exit diameter and u_e is the bulk mean exit velocity.

2.1.4 Three-dimensional nature of flow

The flow reversals within the FPJ chamber are caused by the adverse pressure gradient downstream from the expansion face and the large expansion (Nathan, Hill & Luxton, 1998). However, this reverse flow is not only turbulent, it also exhibits the large-scale coherent precession motion. This distinguishes it from the relatively steady asymmetry that has been observed in channel flows with similar expansion ratios (Ouwa, Watanabe & Asawo, 1981). The investigation of this three-dimensional oscillation in absolute flow direction requires a measurement technique that is able to differentiate direction in the flow velocity, as well as other standard requirements, including adequate spatial resolution and the need to minimise disturbing the flow field of interest. This rules out the use of stationary hot-wire anemometers and pressure probes, which are not able to resolve such turbulent flows reliably. Flying hot-wires, although able to resolve such unsteady flows, are very complex and are difficult to apply to flows within confined cavities. Laser diagnostic tools such as LDA and PIV are considered to be ideal because they are non-intrusive, do not suffer from directional ambiguity when measuring flow velocities (Durst, Melling & Whitelaw, 1981) and can be applied to flows within cavities when adequate optical access is provided.

2.1.5 Bi-directional azimuthal direction

In addition to the oscillation in axial direction of the flow with each cycle, the azimuthal direction of the entire flow can change. Nathan and Luxton (1992), while conducting surface flow visualisation experiments in an FPJ chamber, reported that "for no apparent reason, the surface flow patterns were occasionally destroyed for a short time and then reappeared".

They added that following the reappearance of the flow patterns the precession was reported to sometimes reverse direction in the azimuthal direction. That observation was similarly reported in the numerical simulations of Guo (2000) who explained that the change in precession direction was the result of the phase interaction between the pressure gradient driving the precession and the jet momentum.

2.2 Experimental methodology

Summarising the previous section, the emerging precessing flow is highly three-dimensional and unsteady, with both the exit angle and precession frequency exhibiting considerable cycle-to-cycle variation. To complicate matters, the precession direction and flow mode also change intermittently with time. These flow variations make the flow challenging to study. Laser-based techniques such as LDA and PIV, which were chosen to study the flow field due to their minimally-intrusive nature and capacity to resolve the flow direction, nevertheless have a limited dynamic range. Hence, the simple application of these techniques to such a flow will lead to large uncertainties and also would not provide much information of the 'instantaneous' or phase-averaged structure of the flow. To resolve the flow in a way that accounts for the variations in flow mode, exit angle, precession direction and phase, requires the use of additional flow sensors to condition, or select, the measurements obtained with these laser-based techniques. This type of conditioning allows "phase averaged" data to be recorded, as used successfully by Fick, Griffiths and O'Doherty (1997) to study the precessing vortex core in swirl burners and by Fernandes and Heitor (1998) to measure oscillating flames. Triggering of a PIV data collection system by pressure probes has also been used by Fick, Griffiths and O'Doherty (1997) to study the precessing vortex core near the exit of a swirl burner. A key element to the success of that measurement was the predictability of the precession direction of the PVC. The naturally-excited fluidic precessing jet studied here not only precesses, but is known to change direction intermittently for the Chamber-Lip (Ch-L) configuration (Nathan, 1988). Frequent directional changes in the emerging flow for a Chamber-Lip-Centrebody (Ch-L-CB) configuration were also observed in the LDA tangential velocity measurements (Wong, Nathan & O'Doherty, 2004). It is also numerically predicted by Guo, Langrish and Fletcher (2001) in a long pipe downstream from a sudden expansion inlet. However, those techniques did not require the resolution of precession direction since the directions of these oscillations are predetermined by the physical geometries of the burners. Hence their triggering devices required only one phase sensor. In investigating the unsteady FPJ flow, both precession direction and phase information should be accounted for to provide a suitable trigger to resolve the phase-averaged structure of the jet.

2.2.1 Geometric configuration of the fluidic precessing jet nozzles

The configuration of the FPJ nozzles investigated here is based on the specifications proposed by Hill, Nathan and Luxton (1992) and Hill (1992) for reliable jet precession. A total of nine configurations, each of which give rise to a precessing jet flow, were studied by Wong, Nathan & O'Doherty (2004). Three different inlet conditions were combined with three alternative ways of arranging the FPJ chamber (Wong, Nathan & O'Doherty, 2004). Of these nine, the Ch-L-CB configuration was chosen for further studies because its inlet flow is

uniform and well-defined, and the configuration provides reliable jet precession. Details of these are provided below.

2.2.2 Experimental arrangement

Fig. 2 shows the apparatus used in the experiment, while Fig. 3 shows the geometry of the devices and the coordinate system used for the PIV experiments. A compressor with an operating pressure of up to 650 kPa was used to deliver conditioned and compressed air to the experimental nozzle. The compressed air was regulated to maintain a constant flow rate and was divided into three sub-streams. This was done to provide a flow through the nozzle, while also providing separate seeding both to the nozzle flow and to the entrained air. This avoids the bias that would occur were only the nozzle fluid to be seeded. The first sub-stream was fed into a 6-jet particle generator (TSI Model 9306), while the second sub-stream was diverted to a bypass valve. The two streams were re-combined at the exit of the 6-jet particle generator and transported via a flexible hose into the brass section used to condition the flow. The by-pass arrangement allows the particle generator to function optimally, whilst providing a large air flow rate to the FPJ chamber. The third sub-stream was fed into an in-house-built nozzle particle generator system.

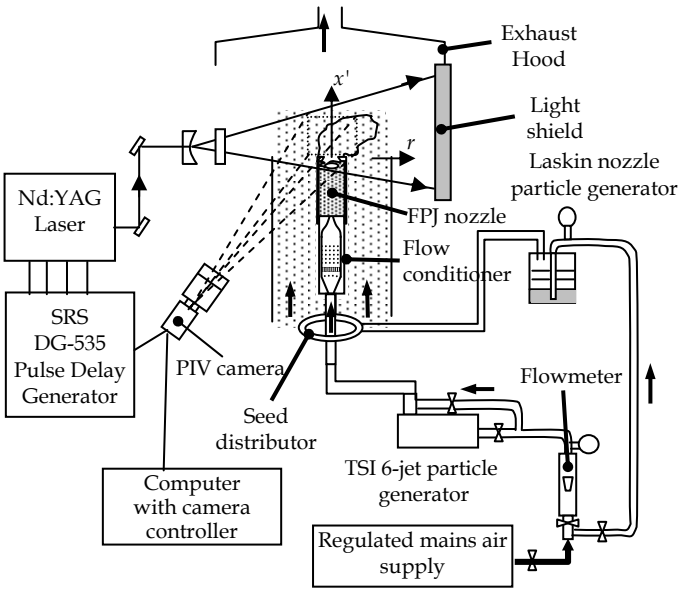

Fig. 2. Experimental arrangement used for PIV experiments. Note that for *x'*-*r* plane experiments, light sheet plane is normal to camera plane as shown. For y-z plane experiments, the camera is directed at an inclined mirror positioned downstream from the FPJ exit plane (not shown here).

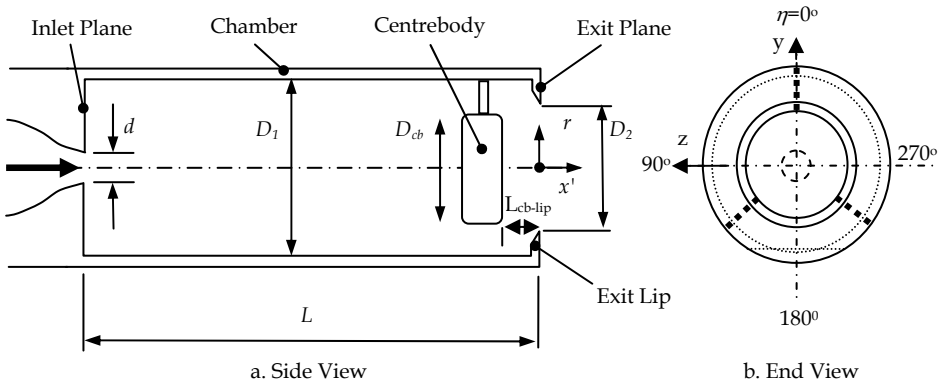

Fig. 3. Coordinate system used in the PIV experiments. d=15.79mm, D_1=80mm, D_2=64mm, D_{cb}=60mm and L=216, t_{cb}=16.8mm, t_{lip}=4mm, $L_{cb\text{-}lip}$=21.6mm and rod diameter of centrebody support is 5mm.

The TSI seeder produces a particle distribution with a modal-mean diameter of 0.6μm, while the nozzle particle generator uses olive oil to generate particle seeding (density, ρ=874kg/m^3 dynamic viscosity, μ=0.026kg/(m.s)) with a nominal particle diameter of approximately 1μm ±0.5μm (Kahler, Sammler and Kompenhans, 2002). Liquid droplets from the nozzle particle generator were used to seed the co-flow around the FPJ chamber and were distributed by means of a ring-type distributor located at the base of the flow conditioner. A cylindrical shroud of about 4.4 times the diameter of the FPJ nozzle was positioned such that the top edge was aligned with the exit plane of the FPJ nozzle. This is used to confine the co-flow seeding within the region of interest. The whole rig is positioned under an exhaust hood which produces a co-flow velocity of about 0.1 m/s based on PIV measurements. To reduce room draughts, all the doors and windows of the experimental laboratory (with a length, breadth and height of 6m, 6m and 5m respectively) were closed.

2.2.3 LDA system

The LDA system is a Dantec two-component LDA system in the burst and back-scatter mode using a Coherent Innova 70 5-W continuous wave Argon-ion laser. In this chapter, only the axial component of velocity is reported here. The 514.5nm (Green) beam line was used. To remove directional ambiguity, one of the split beam line was frequency-shifted by 40MHz. The LDA optical head had a beam separation of 64mm and a focal length of 310mm, resulting in a probe volume with a waist diameter of 0.17mm and a length of 1.65mm. The system was mounted on a Dantec 57G15 three-axis traverse with a position accuracy of ±0.05mm for all axes. Transit-time weighting method of correction was applied to all the velocity data here because a burst mode data sampling was used.

For phase-averaging experiments, a 3-mm diameter open-ended metal tube bevelled at 45° with its bevelled end facing upstream and protruding 10mm into the chamber was mounted half-way between the centrebody and the exit lip. The other end of the tube was connected to a pressure transducer with a 2mV/Pa sensitivity via a 300mm length of PVC tube. The

pressure signal was low-pass filtered at 10 Hz by a 6-pole Butterworth filter and the subsequent signal passed to an oscilloscope which generated a TTL trigger pulse from each falling edge of the filtered pressure pulse. The TTL signal was stored by a Dantec 57N20 enhanced Burst Spectrum Analyser as a false velocity reading that was used a a reference marker for the phase-averaging algorithm. The phase-averaging algorithm divided each 360°-precession cycle into 36 segments based on the reference marker. For each radial measurement location, the axial velocity data in each segment was averaged over each 10°-segment. This technique assumes that the precession mode, precession frequency and phase speed do not change. Variations in these parameters will reduce the measured phase-averaged velocities and will increase the measured *r.m.s.* velocity fluctuations.

2.2.4 PIV experimental arrangement

The PIV system consisted of a light generation system, light delivery system, shaping optics, a pulse delay generator, a PIV camera and suitable lenses.

2.2.4.1 Light generation system

Light was generated by a Quantel Brilliant Twins pulsed Nd:YAG laser system rated at 380mJ per pulse at a frequency-doubled wavelength of 532nm. The Twins has two separate laser systems which produce a fundamental harmonic wavelength of 1064nm. A reference beam and a secondary beam were initially parallel with the secondary beam offset from the reference. The secondary beam was combined down-beam by a series of mirrors and lenses to share a common geometric axis with the primary beam. The combined beams were passed through a second harmonic generator which frequency-doubled the light to generate a (green) wavelength of 532nm. These beams were used in the PIV experiments. Each beam pulse had a manufacturer-specified pulse duration of about 6ns at FWMH (full width at maximum half-height). The short pulse width provided excellent temporal resolution for the current flow. The pulse width duration was also verified by observing on an oscilloscope the electronic signals produced by a high-speed light detector positioned in front of the scattered particles. After optimising the lasers for equal beam strength, the actual power measured was typically 180mJ per pulse per laser cavity for a flashlamp-to-Q-switch delay of 300μs.

2.2.4.2 Light delivery and shaping optics

The laser beam was delivered, via a series of mirrors, to the shaping optics. These comprised a diverging cylindrical lens (focal length 200mm) followed by a cylindrical focusing lens with a focal length of 260mm. Optimising this arrangement of lenses produced a suitable light sheet with a non-uniform thickness that varied between 1mm and 2mm in the region of interest. This thickness was chosen because of the significant out-of-plane motion in the emerging precessing jet. The variation in light sheet thickness was found to have little impact on the results since the calculations for particle out-of-plane motion are based on the minimum light sheet thickness (1mm) and the probe resolutions of the interrogation windows are all larger than the thickest part of the lightsheet (2mm).

2.2.4.3 Pulse delay generator

The laser system comprises two independently-controlled laser oscillators, each of which fire at a nominal rate of 10Hz. The lasers were controlled by a Stanford Research Systems

DG-535 digital pulse delay generator, with a pulse-to-pulse jitter of less than ±5ns. The pulse-to-pulse jitter (or *r.m.s.* fluctuation) between laser pulses was measured to be about ±0.7μs, slightly more than the manufacturer rated jitter of ±0.5μs. This value was used to estimate the precision of the PIV measurements. The pulse delay generator produced a signal whenever an internal timing trigger initiated a timing cycle. The flashlamp-to-Q-switch delay for both lasers was typically set to 300μs to provide a laser energy output of about 180mJ per oscillator. The output signal from the internal timer was sent to the camera which, following an external trigger, had an internal delay of 20μs before exposing the first frame. The exposure time was determined by the transfer pulse width, which was set to 304μs. The first laser pulse was synchronised to illuminate the region of interest during this period. Following this, a transfer pulse delay of 1μs occured before the second exposure was activated for a fixed time period of up to 30ms. The second laser pulse fired at a time Δt after the first pulse to be recorded by frame two. Since a 532nm±10nm narrow bandpass filter was not available, minimum room lighting was used to reduce the effect of background light to negligible levels and background light was later subtracted from each image pair.

2.2.4.4 PIV camera and lenses

The PIV camera was a Kodak Megaplus ES 1.0 (maximum frame-rate of 30Hz), which employed a charged-coupled device (CCD) with an array of 1008 by 1018 pixels (width and height) respectively. The quantum efficiency of the camera is approximately 36% for light at a wavelength of 532nm. Each pixel is approximately 9μm square and has a fill factor of 60%. Each pixel contains three main regions: light sensitive region 1, light sensitive region 2 and a dark region. It was purpose designed to allow it to collect two images in rapid succession. In the "triggered double-exposure mode" or the "frame-straddling mode", light sensitive region 1 is activated to collect photons for an extremely short period. This period, known as the transfer pulse delay, can range from 1 to 999μs. After the transfer pulse delay, a transfer pulse width event occurs before light sensitive region 2 is activated. This time can range from 1 to 5μs. During the transfer pulse width event, integrated light signals falling on region 1 are sequentially shifted into the dark region, which is then further transferred to the random access memory (RAM) of the camera capture card. Light sensitive region 2 is activated for a fixed time of up to 30ms before the data are transferred into the dark region and ultimately into the RAM. Data in RAM are later transferred to permanent storage in local hard disk drives.

The camera was connected to an AF Zoom-Nikkor 70-300mm f/4-5.6D ED lens set at an *f*-number ($f_\#$) of 5.6. The $f_\#$ is the ratio of the focal length, f, to the aperture diameter, D_a. This $f_\#$ value ensured that the image distortion around the edges of the image was minimised, while allowing adequate light to the image array via the lens. Raffel, Willert and Kompenhans (1998) noted that this kind of systematic perspective distortion due to the lens arrangement is generally neglected in most experiments and the only way to quantify this error for highly three-dimensional flows is to measure all three components of velocity. This was not possible using two-component PIV employed in the present investigation.

The depth-of-field of the lens system was checked to ensure that particles within the light-sheet were adequately imaged and focused. The depth-of-field of a lens is the distance along the optical axis over which an image can be clearly focused. For PIV, it is calculated based on the following set of equations from Raffel, Willert and Kompenhans (1998):

$$M = \frac{z_o}{Z_o} \tag{2-1}$$

$$f_{\#} = \frac{f}{D_a} \tag{2-2}$$

$$d_{diff} = 2.44 f_{\#}(M+1)\lambda \tag{2-3}$$

$$\delta_z = \frac{2 f_{\#} d_{diff}(M+1)}{M^2} \tag{2-4}$$

where,

M = magnification factor, z_o = distance between image plane and lens [m]; Z_o = distance between object plane and lens [m]; $f_{\#}$ = f-stop; f = focal length of lens [m]; D_a = aperture diameter [m]; d_{diff} = diffraction limited minimum object diameter [m]; λ= wavelength of light used [m], (532nm for frequency doubled Nd:YAG); δ_z = depth-of-field [m].

To estimate the particle image diameter, the following equation is used neglecting effects of lens aberrations:

$$d_\tau = \sqrt{\left(M d_p\right)^2 + d_{diff}^2} \tag{2-5}$$

where, d_τ = particle image diameter [m] and d_p = particle diameter [m].

The depth-of-field was calculated for each experimental setup, assuming a mean particle diameter of about 1μm, $f_{\#}$ = 5.6, laser wavelength of 532nm, and a nominal image pixel size of 9μm. In general, the depth-of-field exceeds 5.75mm for a magnification (px/mm) of 15. Since all the experiments have light sheet thicknesses of less than 3mm and a magnification of not more than 15px/mm, the depth-of-field used is appropriate and all the particles moving into or out of the light sheet were thus in focus. For a typical magnification of 10.6px/mm, the field-of-view is about 95mm wide by 95mm high.

2.2.5 Phase-and-precession-direction-resolved PIV

Various methods of triggering a data collection system based on external reference conditions have been used by researchers to study time-dependent flows. As noted above, it is necessary to develop a data-collection system that resolves both precession direction and phase. This is achieved with a triggering system using a pair of hot-wire probes to detect the phase and direction of precession. The components to be synchronised are the PIV lasers, the camera system and the triggering system. A block diagram showing the interaction between each system is presented in Fig. 4a while the timing diagram for the trigger system is presented in Fig. 4b.

2.2.5.1 Overall system timing

An ATMEL microprocessor interfaced the laser and camera system with the external hot-wire sensor-trigger system. An important criterion for stable and reliable operation of the

pulsed Nd:YAG laser is that the 10-Hz flashlamp frequency must not vary by more than ±0.5Hz. The laser manufacturer advises that power output decreases dramatically when the flashlamp frequency is outside of the nominal flashlamp frequency (Quantel, 1994).

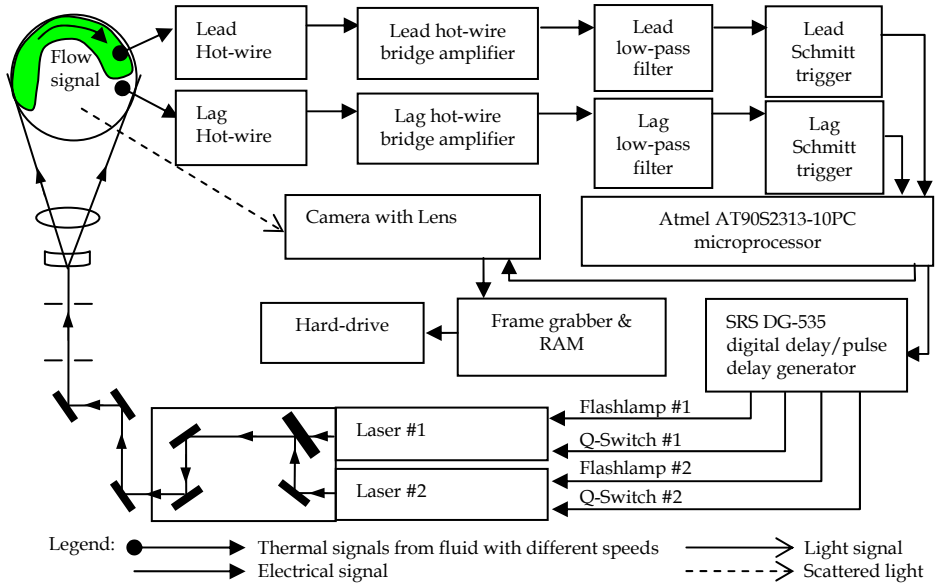

Fig. 4.a. Block diagram of the relationship between the triggers, laser and camera systems.

The following establishes some criteria for the timing system of the microprocessor.

$$f_{fl\_min} < f_{fl\_nom} < f_{fl\_max}\ ;\ 9.5\text{Hz} < f_{fl\_nom} < 10.5\text{Hz}, \text{ and } \delta_{fl\_nom} = 1/\ f_{fl\_nom}.$$

therefore, $$\delta_{fl\_max}=105\text{ms} > \delta_{fl\_nom} > \delta_{fl\_min}=95\text{ms}.$$

where, f_{fl_nom}=Nominal flashlamp frequency [Hz]; f_{fl_min}=Minimum flashlamp frequency [Hz]; f_{fl_max}=Maximum flashlamp frequency [Hz]; δ_{fl_nom}=Nominal flashlamp time interval [sec]; δ_{fl_min}=Minimum flashlamp time interval [sec], and δ_{fl_max}=Maximum flashlamp time interval [sec].

The next step is to choose an appropriate time window that selects a particular band of precession frequency. In the present case, the precession frequency is nominally 5Hz and a frequency range between 3 and 6Hz was chosen. The 3 and 6Hz cut-off frequency range was chosen to match the –3dB frequency interval for a 5Hz precession frequency.

If the frequency range were to be shifted to a higher precession frequency envelope, i.e., from 3 and 6Hz to 4 and 7Hz, fluid structures having a higher precession frequency will be recorded. Although slightly different sizes of structures may be observed, the overall flow topology of the higher precession frequency flow is not expected to be markedly different from the lower frequency flow topology. Data collection time may be increased for the 4 to

7Hz range since the probability of detecting an event decreases as the range is shifted from the –3dB range (located between 3 and 6Hz). This argument similarly applies if the frequency range was shifted to a lower one, such as a range between 2 and 5Hz.

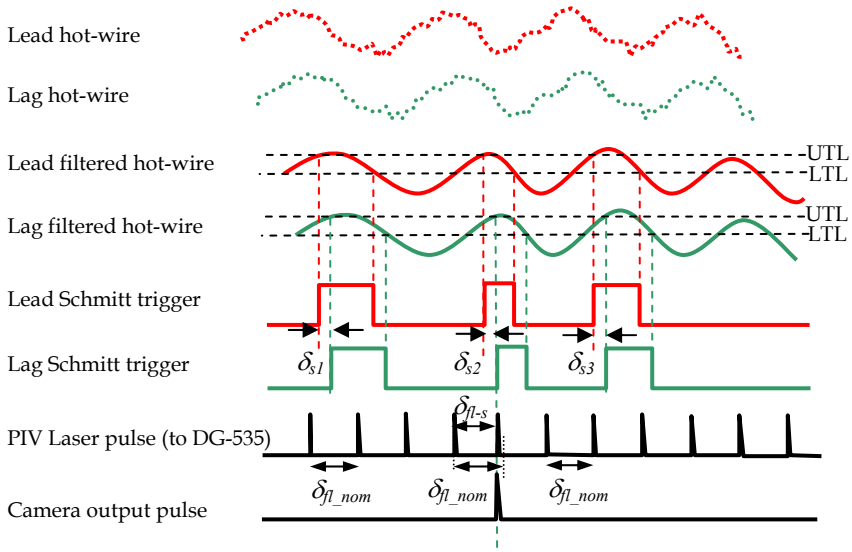

Legend:
UTL: Upper trigger level
LTL: Lower trigger level
Assume δ_{s1} and δ_{s3} are not within the *valid separation time* between Schmitt triggers and δ_{s2} is within the valid separation time between Schmitt triggers

Fig. 4.b. General timing diagram for the phase and precession-direction-resolved PIV experiment.

The main parameters that determined the time window calculations are: linear (or circumferential) separation distance between the two hot-wire probes, radial distance from the hot-wire probe sensing element to the geometric centre of the FPJ, and a frequency bandwidth that characterises the precessing jet (in this case between 3 and 6Hz). The filtering criteria accompanying these parameters are: the jet does not 'flip' across the exit face of the nozzle during one cycle of jet precession, rather the jet takes a circular path about the axis of the chamber, the output from the two-probe arrangement is adjusted to give similar voltage responses to similar velocity fluctuations, and the probes are separated sufficiently to not to interfere with each other.

Following the selection of the frequency bandwidth, a time window for valid inter-trigger times can be set in the microprocessor. The inter-trigger time was the time between triggers that was accepted by the microprocessor as a valid coincidence window for which another comparison can be made with the arrival of a valid laser-trigger. When a valid signal trigger time is sensed after the lag hot-wire probe, an internal comparison is made immediately by the microprocessor to see if a valid laser trigger window has arrived. If there is a match, a

laser trigger and a camera signal are sent simultaneously. If there is no match, the laser trigger will still send a signal to the lasers 100ms after the last known laser trigger, and PIV laser pulses are still produced without the activation of the PIV camera. This was required to maintain stability in the laser system.

2.2.5.2 Atmel microcontroller

The microcontroller employed for this work was an Atmel A90S2313-10PC integrated circuit with a clock frequency of 10MHz. Thus the time resolution for this system can be as small as 0.1μs for each clock cycle. Programming the trigger acceptance window was carried out by transferring the microcontroller to an STK500 programmer's board and downloading the instruction set to the microcontroller's non-volatile memory.

2.2.5.3 Trigger system

Adjustable Schmitt triggers were used to convert the hot-wire signals to TTL-compatible phase pulses with minimal phase lag. Also to minimise the phase lag in the triggering time, short wire-runs were made between the trigger system and the microprocessor. The Schmitt trigger is made from a CMOS 4050 buffer (Lancaster, 1997) with two triggering voltage levels, an upper trigger level (UTL) and a lower trigger level (LTL). Whenever a signal voltage level rises above the upper trigger voltage level, the Schmitt trigger immediately outputs a step change to a high voltage value (+V). If the signal voltage level falls over time, but remains above the lower trigger voltage level, the output continues to remain high. However, when the signal level decreases below the lower trigger voltage level, a step change from high to low (~0V) signal is output from the CMOS 4050 buffer. The region between the trigger levels is known as a "dead band" in which the Schmitt trigger ignores any other voltage signals.

The width of the "dead band" is adjusted with the use of various resistance values (Lancaster, 1997). The use of such a trigger is advantageous to the phase detection of the precessing jet flow because it is possible to trigger the flow on the rising edge of the unfiltered hot-wire signal just before the centre of the jet sweeps past. By using a low-pass filter with a phase lag equal to the time from the trigger to the peak signal region of the jet, it was possible to capture an image of the peak flow coinciding with the physical location of the lag hot-wire probe.

A limitation in the use of the Schmitt trigger is its inability to adjust to variable signal voltage levels. This introduces a "phase jitter band" which varies with fluctuating signal amplitudes. This is estimated to be about ±7° for a repeatable flow (such as a mechanical precessing jet flow) and ±30° for the present FPJ flow. Furthermore, to obtain a small phase jitter band, the upper trigger level had to be set high, so that only a limited large amplitude flow precession would activate the trigger system. This increases the experimental time considerably by reducing the sampling rate (to approximately 1 image for every 300 flow cycles).

2.2.5.4 Verifying the operation of the direction sensors

A simple check was made to verify the direction selectivity of the sensor system with a mechanically precessing jet (MPJ) (Schneider *et al.*, 1997a and 1997b). For brevity, details of the experiment are not shown here; see Wong (2004) for further details. However, the

physical rotation of the MPJ nozzle allows confirmation that the lead hot-wire probe is always exposed to the advancing jet before the lag hot-wire probe. This was found to result in a constant stream of camera signals being sent to the PIV system for data collection, as shown in Fig. 5. To confirm the directional selectivity of the system, the rotation direction of the MPJ was then reversed. This resulted in no triggering of the camera, demonstrating that the system is effective at discriminating precession direction. These experiments also showed that the mean phase lag between the lag hot-wire and the core of the jet is approximately 23.8° with an error band (or jitter) of ±7° as shown in Fig. 5. This phase jitter is caused by several factors, namely, the 3Hz frequency window chosen, the varying exit angle of the jet, and the selection of the UTL of the Schmitt trigger (that relates to the selection of higher magnitudes of velocities before the data collection system is allowed to trigger).

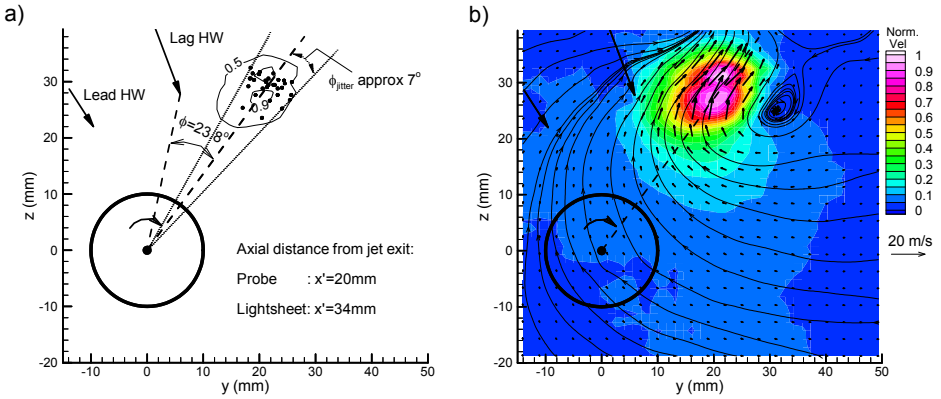

Fig. 5. Verifying the selectivity and phase of the direction sensors with a mechanical precessing jet (d_e=3mm) exiting at θ=45° from the spinning axis rotation in a clockwise fashion at f_p=9Hz. The nozzle is centred at y=0 mm and z=0 mm. **a)** Phase-lag (ϕ) of the jet relative to the lag hot-wire probe, where ϕ_{jitter} refers to phase-jitter in the measurements; **b)** Pseudo-streamlines are shown with velocity vectors while coloured contours represent in-plane velocity magnitudes $(v^2+w^2)^{1/2}$ normalised by $(v^2+w^2)^{1/2}_{max}$=18m/s. Measurements are for a light sheet at x'/d_e =11.3 and probe at x'/d_e =6.7 (and r/d_e=11) for an ensemble of 50 image pairs.

2.2.5.5 Optimising the location of the trigger probes in the FPJ flow

To measure the FPJ flow reliably, a suitable location is needed for the hot-wire probes. Nathan (1988) demonstrated that the introduction of a foreign object (such as a long rod) within the FPJ nozzle cavity will unnecessarily perturb the precessing flow mechanism. In order to avoid this, the probes were positioned outside, but as close as practical to the exit plane of the nozzle to reduce jitter, minimize the interference of the probes and probe holder, and maximize the signal strength of the flow. The lag hot-wire probe was positioned parallel to the nozzle axis with its centre at r/D_2=0.61 in the y-z plane for a total of 4 downstream locations, namely x'/D_2=0.12, 0.25, 0.50 and 0.75. An ensemble average of 50 image pairs are presented in Fig. 6, in which the phase-averaged velocities $(v^2+w^2)^{1/2}$ are non-dimensionalised by the maximum in-plane velocity for each measurement plane and

shown as contours. The difference between each contour level is 0.2. The location of the light sheet was fixed at x'/D_2=0.05. For each experiment, the hot-wire parameters were re-adjusted to suit the new flow conditions for each hot-wire probe location.

The criterion for the best location was chosen by a combination of visual inspection of each successive image pair to decide on the location that results in the least spatial jitter and also by ensemble-averaging the results. In Fig. 6, the locations for x'/D_2=0.12, 0.25 and 0.75 appear to produce similar results in the total magnitude of in-plane velocities. Locating the probe at x'/D_2=0.50 appears to average data over two precession directions, as shown by the larger 'footprint' at the $0.2(v^2+w^2)^{1/2}$ contour. This location coincides with the zone of flow convergence (location of time-averaged, but not instantaneous, flow convergence downstream from the exit plane). Thus, any probe location which senses the magnitude of fluctuating velocities of the emerging precessing jet, other than at a location near to the zone of flow convergence, is a valid choice for the present experiment. The probes were finally located at x'/D_2=0.12 and r/D_2=0.61. This location, which is also approximately 130° to 150° from the peak in-plane velocity magnitude, resulted in the least influence of the probe and probe holder on the overall flow and was not in the plane of the light-sheet. Experiments conducted in the x'-r plane of the local jet centreline show that the instantaneous jet emergence angle (θ=53°) is relatively constant within x'=40mm (or x'/D_2=0.625) (Wong, Nathan & Kelso, 2008). Based on the $0.5(u^2+v^2)^{1/2}{}_{max}$ contours, the range of emergence angles was estimated to be approximately ±15° about the local jet centreline. This range of angles is two times the value of the minimum phase resolution (±30°) in the azimuthal direction (y-z plane) (Wong, Nathan & Kelso, 2008).

2.2.5.6 Selecting the separation distance of the probes

The separation distance between the probes also plays a key role in determining the success of the technique. The lag hot-wire probe was positioned at a radial distance of approximately r/D_2=0.61 and a downstream location of x'/D_2=0.12, as determined from Section 2.2.5.5. To solve for an appropriate probe separation distance, s_c, the following empirical criteria should be satisfied: the highest precession frequency of interest (i.e. 6Hz) should be at least 100 times lower than the smallest clock cycle of the Atmel controller, and the circumferential distance, s_c, travelled by the precessing flow at a fixed radius, r_s, from the nozzle axis should not be more than 10% of the circumference (s_f) described by the radius r_s. That is, $s_c < 0.1\ s_f$.

We can derive the time it takes for the flow to travel between the lead and the lag hot-wire probe (i.e. the separation time, T_{sep}) given the precession frequency of interest (i.e. 3 or 6 Hz), from the following equation:

$$T_{sep} = \frac{s_c}{2\pi r_s f_p} \tag{2-6}$$

Where, s_c = probe separation distance [m], r_s = radial distance between the lag hot-wire probe and the nozzle axis [m], and f_p = precession frequency of interest [Hz].

To calculate the separation time between the lead and lag hot-wire probe for the ATMEL controller time, we use the following conversion formula:

$$T_{atmel} = \frac{T_{sep} \times 10 \times 10^6}{1024} \tag{2-7}$$

The smallest clock resolution (i.e. 1 integer clock cycle) of the ATMEL microcontroller was approximately 0.1ms. Based on the criterion mentioned earlier and for accuracy, a minimum clock time of approximately T_{atmel}=10ms (or 97 clock cycles) for f_p=6Hz was used. Subsequently, T_{atmel}=20ms (or 195 clock cycles) was selected for f_p=3 Hz. The circumference, s_f, travelled by the flow around a circular path for r_s=0.6D_2 is calculated from:

$$s_f = 2\pi r_s \tag{2-8}$$

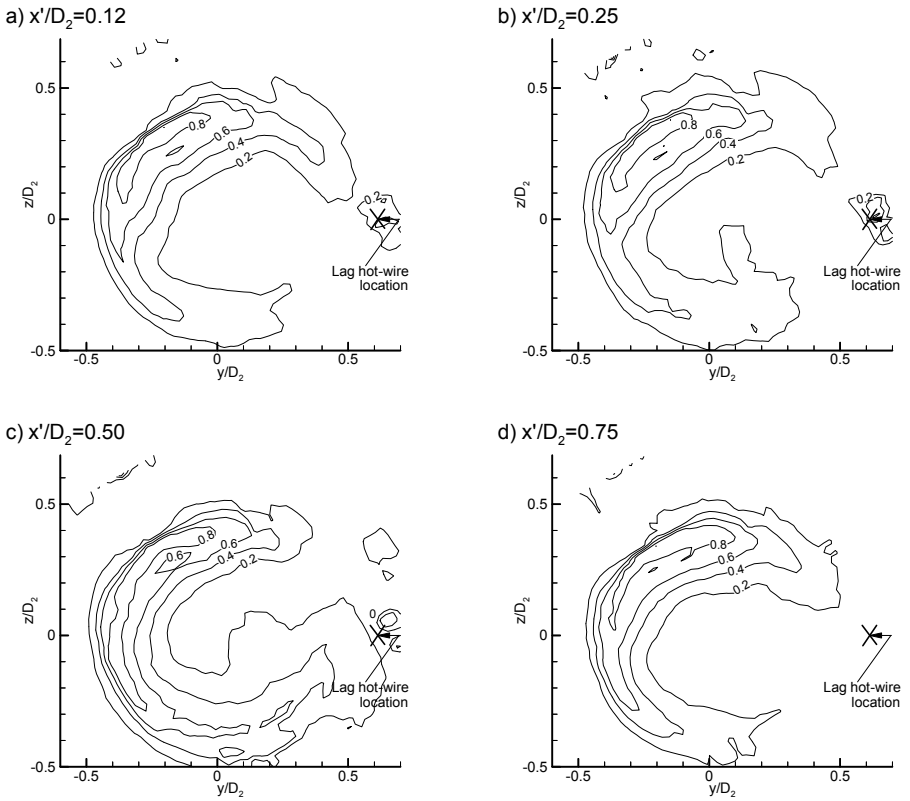

Fig. 6. In-plane velocity magnitude contours, $(v^2+w^2)^{1/2}$, for 4 spatial positions that were tested for the best placement of probes. Velocities are non-dimensionalised by maximum in-plane velocity for respective locations. Precession of the flow from an observer looking upstream is in a clockwise direction. Re_d=59K, St_d=0.00117.

This gives us a circumference of approximately 245mm. If we allow the flow at that radius (r_s) to travel at most 10% of that circumference every cycle, then an appropriate separation distance would need to be less than 24.5mm (that is, an angular separation between the

wires should not exceed 36°). Alternative probe separation distances of s_c=5, 10, 15 and 20mm were also considered. However, for this case, a probe separation of 15mm was chosen as best satisfying the two criteria mentioned earlier.

2.2.5.7 Final setup of the system

The overall PIV system was combined with the phase-and-precession-direction stationary hot-wire sensors. In addition, a Tektronix TDS 210 Real Time Oscilloscope was used to monitor important signal outputs while a PC30D multi-channel A/D converter was used to collect various voltage signals from the Schmitt trigger inputs/outputs, the camera outputs and the laser outputs. The hot-wires were fully annealed prior to the experiments and the hot-wire system was designed for a short warm-up time and turned on at least 2 hours prior to use. If the hot-wire system was not allowed to stabilize, the data collected would be contaminated by electronic drift and lead to a false activation of the Schmitt triggers, and hence introduce errors in the detection of directional flow changes. Both hot-wire probes were held by probe holders and positioned at x'/D_2=0.16 and r/D_2=0.61. They were initially spaced approximately 1mm apart so that they sensed the same magnitude and frequency of flow. Both hot-wire channels (using an overheat ratio of 1.2) were adjusted to respond equally to a 1KHz square wave test. The signals from each hot-wire channel were passed to 4-pole Butterworth (maximally flat) Krohn-Hite filters (Model 3322) and low-pass filtered at the appropriate frequency (30Hz in the present experiments). Both filters were previously adjusted to give the same roll-off and filter frequency response for the same velocity fluctuations. Air was supplied to the FPJ at the experimental condition required and the output of each wire was adjusted to match and to fit within a 0 to +5 volts window. After calibration, the lag hot-wire probe was positioned at a radial distance of approximately r/D_2=0.61, a downstream location of x'/D_2=0.12 and a distance of 15mm from the lead hot-wire probe. Note that time-averaged PIV experiments employed the same experimental arrangement except with the phase-triggering de-activated and the hot-wire system removed.

2.2.6 PIV image pair data processing

Before each experiment, a calibration ruler was positioned within the plane of the laser sheet and its image recorded. This allowed the magnification (in px/mm) of each image to be recorded. An iterative process was then carried out to optimise the experiment so that each run had a velocity data yield of greater than 95%. Firstly, an estimate of the flow velocities was made and a few images taken to assess the relative movement of the correlation peak for a specific interrogation window and a tolerable dynamic velocity range (DVR). The DVR is defined by Adrian (1997) as the ratio of the largest resolvable velocity to the smallest resolvable velocity by the PIV system. An optimum out-of-plane motion of ¼ the lightsheet thickness suggested by Keane and Adrian (1990) was chosen for particles moving perpendicular to the lightsheet. The out-of-plane velocity for the FPJ flow was assumed to be of similar magnitude to the in-plane velocities. The software used for all the image processing, PivView 1.7, was assumed to have a sub-pixel resolution of 0.1 pixel. An acceptable level of cross-correlation signal was achieved by setting the time delay, Δt (typically 10μs), so that an out-of-plane particle motion of ¼ the lightsheet thickness was achieved. Thus, a maximum particle movement of between 3 and 4 pixels was achieved for an interrogation window (IW) of 16x16 pixels with no overlap. A resampling technique after

Hart (2000) reduced the number of spurious vectors due to no overlap used. A global histogram method was used to interactively select the region of interest and to exclude potential outliers. The software stored the 3 highest correlation peaks per correlation calculation. If the highest peak was an outlier, the next highest peak was selected and so on. When a spurious vector was marked, it was replaced by bi-linear interpolation using information from surrounding vectors. When several immediate neighbours were also outliers, then a Gaussian-weighted interpolation scheme was used. The measurement volume was typically 1.5 x 1.5 x 2mm^3 for a scaling of 10.6px/mm, Such small pixel displacements may result in a poor dynamic velocity range in these experiments. Nevertheless, broad features of the flow can still be obtained. A total of 350 image pairs (recorded over 35 seconds) were recorded for the time-average PIV experiments and due to resource limitations 50 image pairs (taking up to 2 hours to collect) were recorded for each phase angle of the phase-average PIV experiment. With only 50 samples collected in the phase-averaged PIV experiment, only the mean data are presented in this chapter.

2.2.7 LDA and PIV experimental uncertainties

Experimental uncertainty calculations follow the method proposed by Martin, Pugliese and Leishman (2000) and Kline and McClintock (1953). For LDA, the calibration uncertainties associated with measurement of probe length, measurement of beam separation and data acquisition uncertainties are approximately ±3.4% of the measured velocity for 95% confidence interval (c.i.). For PIV, the uncertainties associated with camera calibration and jitter in the laser-timing system are approximately ±7% of the measured velocity at 95% c.i.. Other sources of PIV errors (or *r.m.s.* uncertainties) as suggested in Raffel et al (1998) attributable to particle image diameter, particle image displacement, ratio of particle image size and pixel size, particle image shift, image quantisation, background noise of the image, displacement gradients and out-of-plane motions are estimated to be ±1.3% of the measured velocity.

Another major source of error for both techniques is due to phase uncertainties of the jet motion in the azimuthal and axial planes. These were estimated to be ±30° and ±15° respectively for the directionally-resolved phase-averaged PIV experiments, and potentially ±60° and ±15° respectively for the non-directionally resolved phase-averaged LDA experiments. Larger phase uncertainties in both planes contribute to a reduction of the phase-averaged magnitudes compared to velocities obtained during an instantaneous event.

2.2.8 Surface flow visualisation

The purpose of surface flow visualisation is to make visible the patterns of skin-friction lines (Maltby, 1962) and critical points on the surface of (wind-tunnel) models, so that the flow around the surface can be interpreted and understood (Perry & Chong, 1987). This method relies on the response of the visualisation media to skin friction stresses generated by the air-stream flowing over the object's surface, and on the media film being thin enough to be unaffected by pressure gradients (Tobak & Peake, 1979). It should be noted that the response time of this technique is much too long to allow it to represent the instantaneous state of the flow. Instead, the results reflect a pattern caused by the flow's interaction with the surface over a period of time commensurate with the drying time of the media (Hunt et al, 1978). The axial vorticity fields obtained using the phase-precession-direction resolved PIV

revealed the presence of a number of vortical features near to the FPJ exit plane at x'/D_2=0.11. (Wong, Nathan & Kelso, 2008). The presence of these structures was further studied by conducting time-averaged surface flow visualisation on the downstream surface of the centrebody using an alcohol-powder mixture. While these experiments are qualitative, they provide important insight into some of the features measured from the PIV experiments, which do not measure the surface flow field.

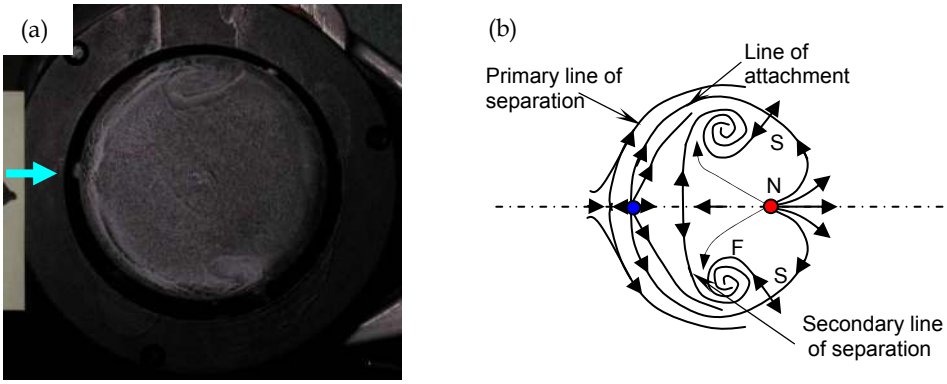

Fig. 7. a) Surface flow visualisation on FPJ nozzle at 10m/s free-stream inlet jet velocity. b) Interpretation of flow topology (Adapted from Wong *et al.* 2008 and reprinted with permission from Cambridge University Press). Steady deflected flow emerging from the left is deflected to the right and emerges at θ~45^o. Re_d~10K, St_d=0. `F′ is focus, `S′ is saddle and `N′ is node.

A steady (non-precessing) jet that deflects at a large exit angle to the nozzle axis was obtained by removing the chamber-section of the FPJ nozzle (chamber-lip-centrebody arrangement) from the supply pipe and introducing an alternative source air at an eccentric location within the inlet plane. The air was supplied by diverting a portion of the flow from a wind tunnel using a suitable turning vane. The deflected air-stream emerging from the exit lip was checked with a cotton tuft attached to a metal rod. As expected, with this arrangement no precession of the jet was detected, but instead the emerging jet was deflected steadily at approximately 45^o relative to the nozzle axis.

Zdravkovich *et al*. (1998) studied coin-like cylinders using a talcum powder-paraffin film mixture; and Potts and Crowther (2000) used kerosene and fluorescent dye powder to study inclined disc-wings. In the present experiments, the use of white talcum powder and methylated spirit (96% ethanol @ 20^{o}C: μ=5.23×10^{-7}kg/(m.s), ρ=802kg/m^3) was found to provide a suitable mixture for surface flow visualization on the centrebody surface. The centrebody and nozzle exit were first painted matt black to provide good contrast from the white powder. The mixture was stirred thoroughly before being applied as a thin and uniform film over the region of interest which was initially positioned horizontally. Excess

mixture was drained off by slightly tilting the model until the desired film thickness was achieved. An optimum film is achieved when the mixture just 'wets' the sample's surface. This was an iterative process as it was difficult to quantify the optimum film thickness due to the rapid evaporation of the methylated spirit. The FPJ nozzle was positioned vertically at the working section with the deflector facing upstream, such that the flow emerging from the nozzle exit plane was deflected by about 45° as indicated by a cotton tuft held by a thin rod positioned in the centre of the exit lip, just above the centrebody.

The most obvious flow features, such as the flow reattachment location and the foci, could be seen to form immediately on the matt black surface of the centrebody (Fig. 7a). More features were revealed as the methylated spirit evaporated over time, leaving only the white talcum powder behind. An interpretation of surface flow topology is shown in Fig. 7b. The influence of the centrebody supports were also considered in the experiments, however, it was found that the orientation of the supports does not greatly affect the distinctive flow patterns observed on the upper surface of the centrebody. As such, a study on the centrebody supports is not further discussed here.

3. Final discussion of key results and issues

3.1 Comparison of time-averaged PIV and LDA results

This section discusses the time-average results for the Chamber-Lip-Centrebody (Ch-L-CB) case for both the 1-D LDA and PIV results. For the LDA experiments, only the jet was seeded and local seeding was applied to seed the ambient fluid during each measurement. This explained the higher validated LDA bursts (nominally 1000) in the locations $-0.7<r/R_2<+0.7$ during the experiments compared to between 10 and 1000 bursts/second outside these locations. Since this configuration was found to generate the precessing jet mode most of the time, any attempts to seed the region near to $r/R_2=0$ was problematic since the presence of the seeding device may have an unwanted influence over the emerging flow. The poor seeding explains a decrease in the LDA burst rate beyond the region $-0.7<r/R_2<+0.7$ in these measurements. However, this did not unduly affect the present results in Fig. 8a and b, (except, for the orifice case) since an acceptable number of validated LDA burst samples (generally greater than 4000) and data rate (at least 10 times higher than the local precession frequency) were achieved. Refer to Wong (2004) for more details. The results of the PIV experiments are also provided in Fig. 8c and Fig. 8d and specific details pertaining to both these experiments are also found in Table 1 and Table 2.

Generally, the axial velocity trends in the PIV and LDA data in the region $-0.8<r/R_2<+0.8$ typically vary by $u/u_i=0.02$. However, in the regions beyond this, the LDA data are expected to over-estimate the true velocity values due to insufficient global seeding. This means that unseeded ambient fluid entrained into the FPJ nozzle will not be recorded, while seeding from the bulk jet will be sampled most of the time. This introduces a velocity bias towards a higher velocity flow, especially in the region beyond $r/R_2=\pm0.8$. Thus, the flow structure beyond the exit lip cannot be elucidated clearly. This is evident in the contrasting results obtained by means of PIV, which employed uniform global seeding instead of localised seeding. The PIV results in Fig. 8c (Mean) and Fig. 8d (RMS) beyond $r/R_2=\pm1.0$ reflect a truer velocity profile as opposed to the LDA results in that region. As explained before, this is due to poor localised seeding beyond the exit lip radius, R_2.

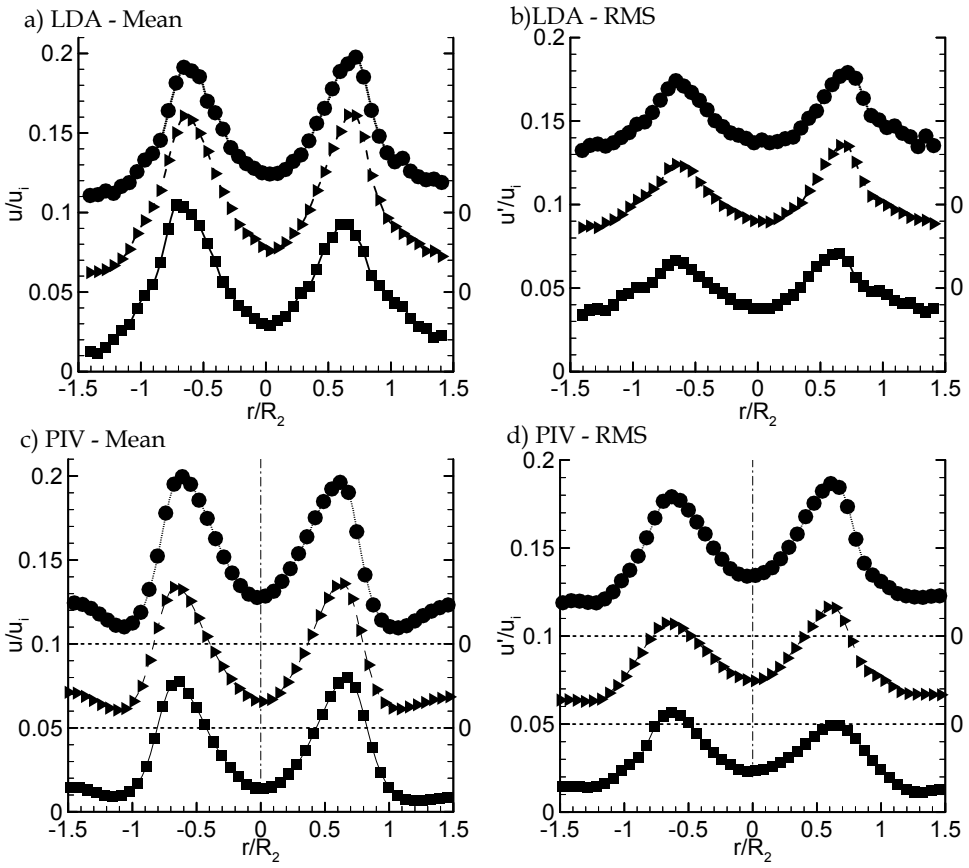

Fig. 8. Comparison between time-averaged LDA and PIV axial velocities at x'/D_2=0.16. The origins of the upwards-shifted ordinates are indicated on the right axis for contraction (▶) and orifice (●) inlets respectively. The left axis refers to the pipe case (■). All velocity values are normalised with the respective bulk inlet velocity u_i, for each inlet case. See Table 1 and Table 2, for LDA and PIV conditions respectively.

3.2 Comparison of conditional-directionally averaged PIV and conditional non-directionally averaged LDA results

Fig. 9a shows the radial distributions of phase-averaged axial velocity at x'/D_2=0.16, obtained using both LDA and PIV techniques. These were measured for Re_d=84,500, St_d=0.0015 and u_i=78.7m/s for the LDA, and Re_d=59,000, St_d=0.0017 and u_i=55m/s for the PIV technique respectively. The closed squares represent the transit-time weighted mean LDA results while the open triangles represent the mean PIV results (obtained at η=60°). Upper and lower confidence intervals (C.I.) at 95% confidence for the PIV measurements are represented as dotted lines and solid lines respectively.

Type of Inlet	Bulk Velocity, u_i m/s	Reynolds Number Based on u_i measured at x/d=1	Average number of LDA bursts per location	Probe volume: axial, radial, tangential (mm)	Step size (mm)
Pipe	103	111,000	13150		2
Contraction	140	150,000	14436	0.17×1.65×0.17	2
Orifice	96	103,000	15465		2

Table 1. Summary of experimental conditions used for the FPJ nozzles measured using LDA.

Type of Inlet	Bulk Velocity, u_i m/s	Reynolds Number based on u_i and d measured at x/d=1	N	Probe dimensions: axial, radial, tangential (*mm*)	Step size: axial, radial, mm	Δt (μs)	px/mm
Pipe	34.5	37,100	700	3.39×3.39×2	1.74	10	9.45
Contraction	29.7	31,900	1049	3.59×3.59×2	1.82	12	8.91
Orifice	26.4	28,400	1047	3.68×3.68×2	1.9	12	8.69

Table 2. Summary of experimental inlet conditions, in the absence of the nozzle chamber, used for the FPJ nozzles measured in time-averaged PIV experiments.

The phase-averaged LDA results broadly agree well, in terms of profile shapes and velocity magnitudes, with the PIV results within the range $-0.5 \le r / D_2 \le 0.1$. The LDA velocity measurements are generally larger than the PIV velocity measurements in the ranges $-0.48 < r/D_2 < -0.5$ and $r/D_2 > +0.1$. This can be explained by the differences in seeding methods. In the LDA experiments, the co-flow was only seeded from one local azimuthal location, i.e. it was seeded asymmetrically, so that the two measurements agree well for the side that was well seeded. However, the LDA will over-estimate the velocity for the region in which the ambient fluid was poorly seeded, so was subject to a velocity bias. In contrast, the seeding in the PIV experiment was uniform in the azimuthal direction.

In general, as shown in Fig. 9a, the axial velocity trend using both techniques rises from u/u_i=0 near to r/D_2= - 0.5 and peaks at approximately u/u_i=0.10, after which it decreases to a minimum near to r/D_2=+0.1 before rising again to a second maximum of u/u_i~0.085 at r/D_2=+0.30 for the PIV measurements and u/u_i~0.04 at r/D_2=+0.38 for the LDA measurements. There is an apparent shift of the second peak for the LDA results and also a decrease in the LDA axial velocities between $0.1 < r/D_2 < 0.4$, despite transit-time weighted corrections to account for velocity bias. These differences may be attributed to a better phase and directional accuracy for the PIV measurements than for the LDA measurements.

Fig. 9b and Fig. 9c present the radial distributions of the phase-averaged PIV and LDA results for downstream locations at x'/D_2=0.48 and 0.79 respectively. Again, both techniques show similar axial velocity trends and have comparable velocity magnitudes, differing only

by u/u_i=0.02 and 0.035 respectively. The larger magnitudes in the LDA results relative to the PIV measurements on the right-hand side of the jet are attributed to LDA velocity bias towards the higher velocities, as discussed above, noting also that the effectiveness of the external seeding of the measurement region decreases with distance downstream from the FPJ exit plane. Again, these differences may also be attributed to a better phase and directional accuracy for the PIV measurements than for the LDA measurements.

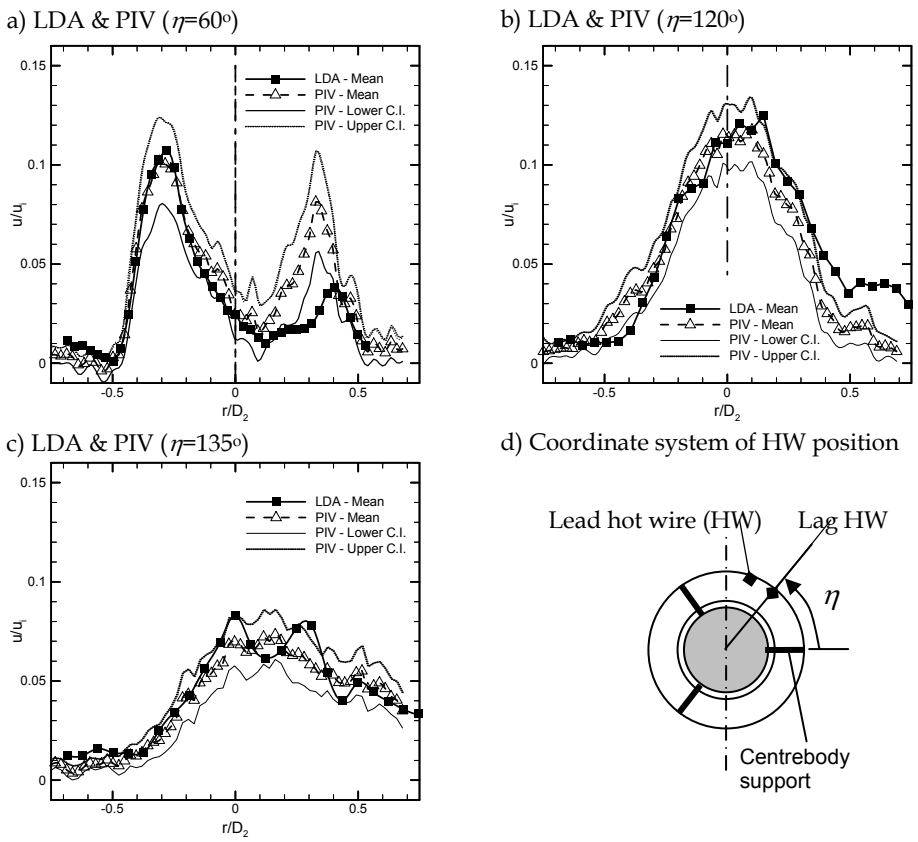

Fig. 9. Comparison between phase-averaged LDA and PIV axial velocities at x'/D_2=0.16, 0.48 and 0.79. Shown also are lower and upper 95% confidence interval (C.I.) for PIV results. Axial velocities are non-dimensionalised by u_i=78.7m/s for LDA and u_i=55.0 m/s for PIV. LDA:Re_d=84,500 and St_d=0.0015. PIV:Re_d=59,000 and St_d=0.0017.

3.3 Construction of flow topology

Fig. 10 illustrates the development of the 0.50 and 0.9 $(v^2+w^2)^{½}{}_{x',max}$ contours for various downstream sections from the exit lip taken from phase-averaged PIV measurements in the y-z plane. The jet is initially kidney-shaped (Fig. 10a), but as it converges to x'/D_2=0.58 (Fig.

10 f), it becomes an almost round jet. The approximate trajectory of the jet centreline in the transverse cross-section initially deflects to the left of the advancing side of the jet, but this deflection is most noticeable after the convergence location at approximately x'/D_2= 0.58.

Wong, Nathan and Kelso (2008) summarised the important features identified in the phase-averaged longitudinal (x'-r plane) PIV results. These were, a saddle above a reversed flow region near to the exit plane in the central region of the nozzle, a region of separation on the surface of the exit lip whereby the head of the focus points inwards, the mean extent of the flow convergence region, a region of separation on the surface of the exit lip where the head of the focus points outwards, and a conjectured streamline pattern describing the structure of an Edge 2 and an Edge 3 vortices. Some of these features are shown in Fig. 11a.

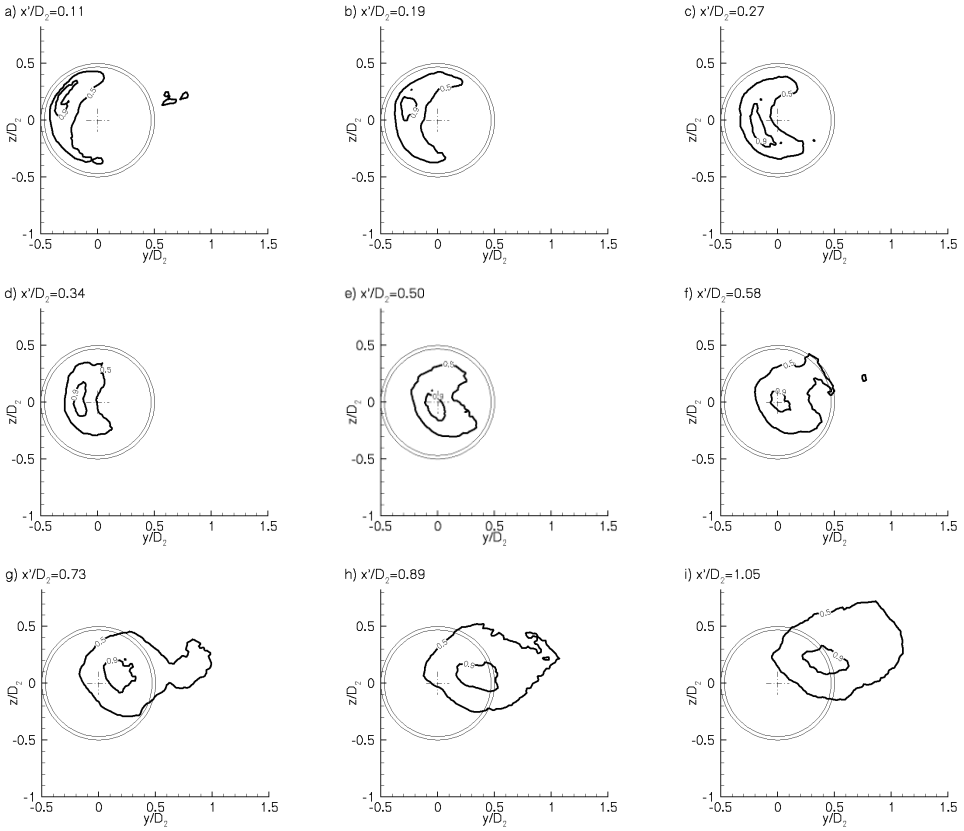

Fig. 10. Cross-sectional development of the jet downstream showing 0.5 and 0.9 $(v^2+w^2)^{½}{}_{x',max}$ contour levels. Note that by x'/D_2=0.58, the jet is almost round. D_2=64mm. Re_d=59K, St_d=0.0017.

The pair of vortices emerging from the middle of the centrebody represents the centrebody (CB) vortex pair which originate from the foci located to either side of the centrebody surface. These vortices move closer to each other with downstream distance and finally annihilate one another by $x'/D_2 \sim 0.5$. The thin black dashed line represents the vortex that is thought to originate from the edge of the centrebody (that is, the Edge 1 vortex). The 'legs' of this vortex form a pair of longitudinal vortices downstream of the centrebody (the Edge 1 vortex pair). These appear as positive and negative vorticity regions as seen by a downstream observer. This vortex pair departs the centrebody at an inclined angle, cutting the lower measurement planes at a large angle. Thus, the vortex pair appears as two kidney-shaped patterns near to the leading edge of the high velocity jet stream in the vorticity results of the transverse PIV measurements as given in Fig. 11a. Wong, Nathan and Kelso (2008) showed that the negative leg of this Edge 1 vortex follows the trajectory of the jet fairly closely. The positive Edge 1 vortex is initially located in the vicinity of y/D_2=+0.1 and z/D_2=+0.4, but at a distance x'/D_2=0.58 it moves towards y/D_2=+0.6 and z/D_2=+0.15 with increasing radius from the nozzle axis while departing in a direction opposite to the jet precession.

The thin blue solid line in Fig. 11c represents the core of a vortex that sits slightly above the surface of the exit lip and then lifts away from the exit at the rear side of the exiting jet (opposite the side from which the jet emerges). The lift-off occurs at an azimuthal angle of 130° to 150° from the center of the emerging jet. The legs of this lifted vortex form the 'Edge 2 vortex pair'. The vorticity associated with this vortex is observed most clearly in the longitudinal phase-averaged PIV experiments provided in Fig. 11b. The emerging jet separates at the exit lip to form a saddle-focus pattern at r/D_2=0.6 at x'/D_2=0.05 as illustrated in Fig. 11b. This pattern appears to be generated by the separation of the external flow entrained along the outside surface of the FPJ nozzle, and the separation of the exiting FPJ flow at the edge of the lip. The focus seen in Fig. 11b has a direction of rotation (clockwise) that is consistent with the vorticity that would be shed from the outer surface of the FPJ.

By inspection of Fig. 11a, Fig. 11b and the conjectured topology of Fig. 11c, the Edge 1 vortex and the Edge 2 vortex are of the same sign of circulation. If the emerging jet were to depart along the geometric axis (i.e. without deflection), then the Edge 2 vortex should remain in a closed 'circular' loop (or ring) sitting above the exit lip. However, the asymmetry of the emerging jet causes one end of this vortex loop to be entrained into the emerging jet flow between approximately 130° and 150° ahead of the advancing jet (Wong, Nathan & Kelso, 2008). This range of angles is similar to the separation angles of the surface flows in jets in crossflow (Fric & Roshko, 1994). Thus the edge vortex forms a horseshoe-shaped loop with either side of the loop being entrained into the advancing and receding sides of the jet. The lift-up of the Edge 2 vortex 'pair' from the surface of the exit lip appears initially to influence the trajectory of the Edge 1 vortex. The trajectories of the two 'legs' of the Edge 2 vortex follow the same trend as the Edge 1 vortex, in terms of the y-z trajectory with downstream distance, albeit with a slight delay in phase. The presence of the Edge 2 vortex pair below the core of the jet was detected in earlier phase-averaged LDA studies (Wong *et al*., 2003) and in the $0.5(v^2+w^2)^{1/2}{}_{max}$ velocity contours of the phase-and-precession-direction-resolved PIV studies (see Fig. 10g).

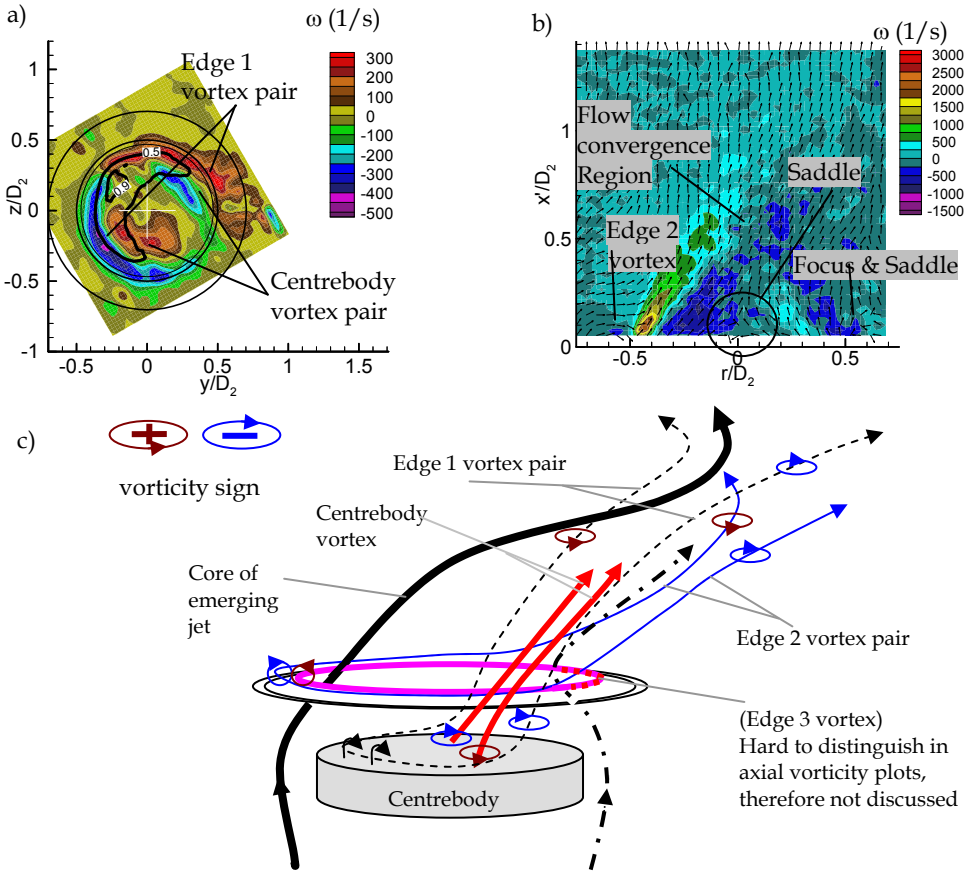

Fig. 11. Typical vorticity fields in the a) *y-z* plane @ x'/D_2=0.19 and b) *x'-r* plane @ η=60°. c) Qualitative interpretation of experimental data. (Adapted from Wong *et al.* 2008 and reprinted with permission from Cambridge University Press).

4. Conclusion

The study illustrates that a pre-requisite to the detailed application of laser diagnostic tools such as PIV and LDA is an adequate understanding of the qualitative features of the flow of interest. This is necessary for the design and careful application of appropriate triggering conditional statistics. When dealing with turbulent flow coupled with time-variant three-dimensional fluidic oscillations, it is important to match the flow conditions with the technical limits of the flow instrumentation. For the investigation of the fluidic precessing jet flow, the Schmitt filter was found to be effective in allowing two carefully-placed hot wire probes to provide a trigger to discriminate for both phase and direction of the oscillation, both of which vary randomly. This trigger allowed resolution of the azimuthal component of the flow velocity in the PIV data, which were smoothed out in the LDA measurements and also triggered on phase only, and not on direction. For the measurement of unconditioned statistics, such as the mean and *r.m.s.* statistical quantities, good agreement was found here between the PIV and LDA techniques for those regions of the flow in which both techniques were well seeded. As expected, some disagreements were found in those regions of the flow in which the seeding of the ambient air was poor, due to the non-uniform seeding technique, where the strong entrainment of unseeded ambient fluid led to a systematic velocity bias for the LDA case.

5. Acknowledgment

The authors acknowledge the Australian Research Council, Schools of Mechanical and Chemical Engineering (University of Adelaide) and Division of Mechanical Engineering (University of Wales, Cardiff) for various in-kind assistance, equipment and facility support. CYW also acknowledges the International Postgraduate Research Scholarship that enabled this research to be conducted. The authors are also grateful to the various peer-reviewers who have reviewed this manuscript.

6. References

Adrian R.J. (1997) Dynamic ranges of velocity and spatial resolution of particle image velocimetry. *Meas. Sci. Technol.*, 8, pp.1393-1398.

Durst F., Melling A. & Whitelaw J.H. (1981) *Principles and practice of laser-Doppler anemometry.* Academic press, London.

Fernandes E.C. & Heitor M.V. (1998) On the extension of laser-Doppler anemometer to the analysis of oscillating flames. In, *Proc. 9th Int. Sym. On Appl. Laser Techniques to Fluid Mechanics*, Lisbon, Portugal, 1, pp.3.3.1-3.3.9, 13-16 July.

Fick W., Griffiths A.J. & O'Doherty T. (1997) Visualisation of the precessing vortex core in an unconfined swirling flow. *Optical Diagnostics in Engineering*, 2(1), pp.19-31.

Fric T.F. & Roshko A. (1994) Vortical structure in the wake of a transverse jet. *J. Fluid Mech.*, 279, pp.1-47.

Guo B.Y. (2000) *CFD simulation of flow instability in axisymmetric sudden expansions*. PhD Thesis, Dept. of Chem. Eng., The University of Sydney, Australia.

Guo B.Y., Langrish T.A.G. & Fletcher D.F. (2001). Numerical simulation of unsteady flow in axisymmetric sudden expansions. Trans. ASME, *J. Fluids Eng.*, 123, pp.574-587, September.

Hart D.P. (2000) PIV error correction. *Exp Fluids*, 29, pp.13-22.

Hill S.J. (1992). *Characterisation of the flow fields produced by the enhanced mixing nozzle: A development towards high temperature and multi-phase applications*. Internal report, Dept. Mech. Eng., University of Adelaide.

Hill S.J., Nathan G.J. & Luxton R.E. (1992). Precessing and axial flows following a sudden expansion in an axisymmetric nozzle. In, *Proc. 11th Australiasian Fluid Mechanics Conference*, University of Tasmania. Hobart, Australia, pp.1113-1116, 14-18 December.

Hill S.J., Nathan G.J. & Luxton R.E. (1995). Precession in axisymmetric confined jets. In, Bilger R.W., editor, *Proc. 12th Australasian Fluid Mechanics Conference*, Sydney, pp.135-138, 10-15 December.

Hunt J.C.R., Abell C.J., Peterka J.A. & Woo H. (1978). Kinematical studies of the flows around free or surface mounted obstacles; applying topology to flow visualization. *J. Fluid Mech*., 86, pp.179-200.

Kähler C.J., Sammler B. & Kompenhans J. (2002) Generation and control of tracer particles for optical flow investigations in air. *Exp. Fluids*, 33, pp.736-742.

Keane R.D. & Adrian R.J. (1990). Optimization of particle image velocimeters. Part I: Double pulsed systems. *Meas. Sci. Technol*., 1, pp.1202-1215.

Kline S.J. & McClintock F.A. (1953) Describing uncertainties in single-sample experiments. Mechanical Engineering, 75, pp. 3-8, Jan.

Lancaster D. (1997). *CMOS Cookbook, Second Edition*. Newnes, United States of America.

Luxton R.E. & Nathan G.J. (1988). *Mixing of fluids*, Australian Patent Office (Patent Application No. 16235/88, International Patent Application No. PCT/AU88/00114).

Maltby R.L. (1962). *Flow visualization in wind tunnels using indicators*. AGARDOGRAPH, No.70.

Manias C.G. & Nathan G.J. (1994). Low NO_x clinker production. *World Cement*, 25(5), pp.54-56, May.

Martin P.B., Pugliese G.J. & Leishman J.G. (2000) Laser Doppler velocimetry uncertainty analysis for rotor blade tip vortex measurements. *AIAA 2000-0263*, 15pp.

Mi J. & Nathan G.J. (2000). Precession Strouhal number of a self-excited precessing jet. In, Ping Cheng, Ed., *Proc. Symposium on energy engineering in the 21st Century (SEE2000)*, Begell House, Hong Kong, 4, pp.1609-1614.

Mi, J., & Nathan, G.J. (2005) "Statistical analysis of the velocity field in a mechanical precessing jet flow", *Physics of Fluids*, 17, (1), 015102, 1-17.

Nathan, G.J. (1988) *The enhanced mixing burner*. PhD thesis Dept of Mech Eng, Uni of Adelaide, Australia.

Nathan G.J., Hill S.J. & Luxton R.E. (1998) An axisymmetric 'fluidic' nozzle to generate jet precession. *J. Fluid Mech.*, 370, pp.347-380.

Nathan G.J. & Luxton R.E. (1992) The flow field within an axi-symmetric nozzle utilising a large abrupt expansion. In, Zhuang F.G., editor, *Recent advances in experimental fluid mechanics*, International Academic Publishers, pp.527-532.

Nathan G.J., Mi, J., Alwahabi, Z.T. Newbold, G.J.R. & Nobes, D.S. (2006) Impacts of a jet's exit flow pattern on mixing and combustion performance, *Prog. Energy Combust. Sci.*, 32, (5-6), 496-538.

Newbold G.J.R. (1997) *Mixing and combustion in precessing jet flows*, Ph.D. Thesis, Dept. Mech. Eng., The University of Adelaide, Australia.

Nobes D.N. (1997). *The generation of large-scale structures by jet precession*, Ph.D. Thesis, Dept. Mech. Eng., The University of Adelaide, Australia.

Quantel (1994). *Quantel twins Q-switched double pulse Nd:YAG laser. Instruction manual issue no.1.* Quantel, France, May.

Ouwa, Y., Watanabe, M. & Asawo, H. 1981 Flow visualisation of a two dimensional water jet in a rectangular channel. *Japan. J. Appl. Phys.* 20, 243-247.

Parham, J.J. (2000). *Control and Optimisation of Mixing and Combustion from a Precessing Jet Nozzle*, Ph.D. Thesis, Dept. Mech. Eng., The University of Adelaide, Australia.

Perry A.E. & Chong M.S. (1987). A description of eddying motions and flow patterns using critical-point concepts. *Ann. Rev. Fluid Mech.*, 19, pp.125-155.

Potts J.R. & Crowther W.J. (2000). The flow over a rotating disc-wing. In, *Proc. Royal Aeronautical Society Aerodynamics Research Conference*, London, UK, Apr.

Raffel M., Willert C. & Kompenhans J. (1998) *Particle image velocimetry – a practical guide*. Springer, Germany.

Schneider G.M., Froud D., Syred N., Nathan G.J. & Luxton R.E. (1997a) Velocity measurements in a precessing jet flow using a three dimensional LDA system. *Exp. Fluids*, 23, pp.89-98.

Schneider G.M., Hooper J.D., Musgrove A.R., Nathan G.J. & Luxton R.E. (1997b) Velocity and Reynolds stresses in a precessing jet flow. *Exp. Fluids*, 22, pp.489-495.

Tobak M. & Peake D.J. (1979). Topology of two-dimensional and three-dimensional separated flows. In, *Proc. AIAA 12th Fluid and plasma dynamics conference*, Williamsburg, Virginia, USA, 79-1480, 23-25 July.

Videgar R. (1997). Gryo-therm technology solves burner problems. *World Cement Case Studies*, Nov.

Wong C.Y., Lanspeary P.V., Nathan G.J., Kelso R.M. & O'Doherty T. (2003). Phase-averaged velocity in a fluidic precessing jet nozzle and in its near external field. *J. Exp. Therm. Fluid Sci.*, 27, pp.515-524.

Wong, C.Y. (2004) *The flow within and in the near external field of a fluidic precessing jet nozzle*. Ph.D Thesis, Department of Mechanical Engineering, The University of Adelaide, Australia.

Wong, C.Y., Nathan, G.J. & O'Doherty, T. (2004). The effect of initial conditions on the exit flow from a fluidic precessing jet nozzle. *Exp. Fluids*, 36, pp.70-81.

Wong C.Y., Nathan G.J. & Kelso R.M. (2008) The naturally oscillating flow emerging from a fluidic precessing jet nozzle. *J. Fluid Mech.*, 606, pp.153-188.

Zdravkovich M.M., Flaherty A.J., Pahle M.G. & Skelhorne I.A. (1998). Some aerodynamic aspects of coin-like cylinders. *J. Fluid Mech*., 360, pp.73-84.

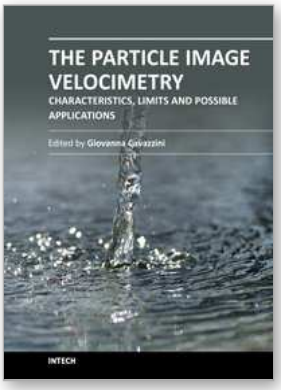

The Particle Image Velocimetry - Characteristics, Limits and Possible Applications

Edited by PhD. Giovanna Cavazzini

ISBN 978-953-51-0625-8
Hard cover, 386 pages
Publisher InTech
Published online 23, May, 2012
Published in print edition May, 2012

The Particle Image Velocimetry is undoubtedly one of the most important technique in Fluid-dynamics since it allows to obtain a direct and instantaneous visualization of the flow field in a non-intrusive way. This innovative technique spreads in a wide number of research fields, from aerodynamics to medicine, from biology to turbulence researches, from aerodynamics to combustion processes. The book is aimed at presenting the PIV technique and its wide range of possible applications so as to provide a reference for researchers who intended to exploit this innovative technique in their research fields. Several aspects and possible problems in the analysis of large- and micro-scale turbulent phenomena, two-phase flows and polymer melts, combustion processes and turbo-machinery flow fields, internal waves and river/ocean flows were considered.

INTECH
open science | open minds

InTech Europe
University Campus STeP Ri
Slavka Krautzeka 83/A
51000 Rijeka, Croatia
Phone: +385 (51) 770 447
Fax: +385 (51) 686 166
www.intechopen.com

InTech China
Unit 405, Office Block, Hotel Equatorial Shanghai
No.65, Yan An Road (West), Shanghai, 200040, China
中国上海市延安西路65号上海国际贵都大饭店办公楼405单元
Phone: +86-21-62489820
Fax: +86-21-62489821